IEEE Access
Multidisciplinary | Rapid Review | Open Access Journal

Received January 26, 2022, accepted February 9, 2022, date of publication February 11, 2022, date of current version February 18, 2022.

Digital Object Identifier 10.1109/ACCESS.2022.3151049

Fast Scattered Far-Field Predictions for Super-Resolution ISAR Image Formation Using the Shooting and Bouncing Ray Technique

JAE-IN LEE AND DONG-WOOK SEO, (Senior Member, IEEE)
Interdisciplinary Major of Maritime AI Convergence, Korea Maritime and Ocean University, Busan 49112, Republic of Korea

Corresponding author: Dong-Wook Seo (dwseo@kmou.ac.kr)

This work was supported by the Basic Science Research Program through the National Research Foundation of Korea (NRF) funded by the Ministry of Education under Grant 2021R1I1A3044405.

ABSTRACT It is essential to obtain a large amount of inverse synthetic aperture radar (ISAR) image data for ISAR automatic target recognition. For a super-resolution ISAR image for a complex perfect electric conducting (PEC) computer-aided design (CAD) model, parameter estimation methods should be applied to $M \times N$ scattered far-field data over M frequencies and N angles, which is conventionally obtained by using the shooting and bouncing ray (SBR) technique. Therefore, N-time ray tracing processes are required for N angles, and $M \times N$-time field calculations are required for M frequencies. In this paper, to reduce the computation time for $M \times N$-time field calculations, we introduce a fast scattered far-field prediction method for a super-resolution ISAR image of a complex PEC CAD model using the SBR technique. This method consists of two main ideas. First, under the small-angle approximation, we derive a DFT-based ISAR image formula in closed form, which allows the rapid acquisition of DFT-based ISAR image through just a one-time ray tracing process at the center frequency and angle. In addition, the scattered far-field data are also obtained by inverse discrete Fourier transforming the DFT-based ISAR image without N ray tracing processes and $M \times N$ field calculations. Second, a field truncation method is employed to suppress errors in the scattered far-field data caused by the proposed closed-form formula. Further, by applying a parameter estimation method to the scattered far-field data, a super-resolution ISAR image is obtained quickly. Simulation results for complex PEC CAD models are in good agreement with the results for the conventional method, while the computation times are tremendously reduced.

INDEX TERMS Far-field calculation, one-shot ISAR imaging, super-resolution ISAR imaging, shooting and bouncing ray (SBR) technique, scattering center extraction.

I. INTRODUCTION

Synthetic aperture radar (SAR) and inverse synthetic aperture radar (ISAR) images are important radar signatures for analyzing the electromagnetic scattering properties of large and complex targets. In SAR automatic target recognition (ATR), a SAR/ISAR image of an unknown target is recognized by comparing it to simulated SAR/ISAR images of many computer-aided design (CAD) models [1], [2]. For one CAD model, hundreds of SAR/ISAR images are required, so rapid calculation time for the SAR/ISAR image is an important issue in SAR ATR.

In the conventional methods of simulating an ISAR image for a CAD model, the ISAR image is obtained by Fourier transforming monostatic scattered far-field data over multiple frequencies and angles [3]. If M and N are the numbers of observation frequencies and angles, respectively, $M \times N$ monostatic scattered far-field data are required for one ISAR image. The shooting and bouncing rays (SBR) technique, one of the asymptotic high-frequency methods, is mainly used to calculate the scattered far-field data because of its fast calculation time [4], [5]. The SBR technique is performed through the following steps. A dense grid of rays, which describes the incident wave, is launched into a perfect electric conducting (PEC) CAD model, and each ray is traced according to the geometrical optics (GO) principle. Finally,

The associate editor coordinating the review of this manuscript and approving it for publication was Guido Lombardi.

the scattered far-field is calculated by the physical optics (PO) integration at the last hit point of each ray. Although scattered far-field at a given frequency and angle can be calculated quickly using the SBR technique, it is time-consuming to perform the ray tracing process N times and to calculate the scattered field $M \times N$ times over M frequencies and N angles.

Under the small-angle approximation, the computation time of the N-time ray tracing processes can be effectively reduced by utilizing the monostatic-bistatic equivalence (MBE) principle [6], [7]. The monostatic scattered far-field data over N angles are calculated from the bistatic scattered far-field data through just a one-time ray tracing process at the center angle. Therefore, for one ISAR image, ray tracing is performed just once at the center frequency and angle. Although the MBE principle is an efficient way to reduce the number of ray tracing for PEC targets under the small-angle approximation, $M \times N$-time field calculations is still a big burden to obtain one ISAR image.

To solve this field calculation problem, an image-domain ray-tube integration formula was derived that directly computes the ISAR image and skips the calculation of the scattered far-field data [8]–[15]. By using the formula, the contribution of each ray to the ISAR image is directly calculated through just a one-time ray tracing process at the center frequency and angle, and the ISAR image is obtained quickly by summing up the contribution of each ray. This method reduces computation time tremendously, but it has limitations due to the Fourier transform (FT) characteristics.

An FT-based ISAR image has a limited range resolution, and the scattering center has sidelobes in the FT-based ISAR image domain. These limitations make it difficult to analyze the scattering properties of a CAD model. The sidelobes can be suppressed using the scattering center extraction algorithm based on CLEAN [16]–[20]. However, there is a possibility of extracting spurious scattering centers that worsen the performance of SAR ATR, and the limited range resolution still exists.

Therefore, super-resolution ISAR imaging methods have been studied using parameter estimation methods such as MUSIC and ESPRIT [21]–[26]. These methods extract scattering centers exactly in super-resolution and solve the problems caused by the FT-based ISAR imaging method. To apply the parameter estimation methods, $M \times N$ scattered far-field data must first be obtained. However, the image-domain ray-tube integration formula [9] is only used to obtain the FT-based ISAR image and is unsuitable for quickly obtaining the $M \times N$ scattered far-field data and the super-resolution ISAR image.

In this paper, we propose a fast simulation algorithm for obtaining a super-resolution ISAR image for a complex PEC CAD model using the SBR technique. That is, we propose the fast scattered far-field prediction method, which is based on two main ideas. First, a discrete Fourier transform (DFT)-based ISAR image formula is derived in closed form under the small-angle approximation. This proposed formula is a modified image-domain ray-tube integration formula. By using the proposed formula, the DFT-based ISAR image is obtained quickly through just a one-time ray tracing process at a center frequency and angle, and scattered far-field data are quickly obtained by inverse discrete Fourier transforming the DFT-based ISAR image. Second, a field truncation method is proposed to suppress errors in the scattered far-field data caused by the proposed closed-form formula. Therefore, scattered field data with few errors are obtained quickly by using the proposed formula and the field truncation method. Further, by applying a parameter estimation method to these field data, a super-resolution ISAR image is obtained quickly.

This paper is organized as follows. Section II briefly reviews the SBR, MBE, and parameter estimation methods required to derive the closed-form formula for the DFT-based ISAR image in Section III. Additionally, we introduce the filed truncation method to suppress the errors. In Section VI, we verify the validity of the proposed method through simulated results for two CAD models. Finally, some conclusions are drawn in Section IV.

II. BRIEF REVIEW OF SBR TECHNIQUE, MBE PRINCIPLE, AND PARAMETER ESTIMATION METHODS

In this section, we briefly review the SBR technique, the MBE principle, and how we apply the parameter estimation methods to the field data. These explanations are necessary to derive the proposed formula, which is the closed-form formula for the DFT-based ISAR image.

A. THE SHOOTING AND BOUNCING RAYS TECHNIQUE

As mentioned in Section I, the SBR technique determines information for the last hit points of rays by launching a dense grid of rays and tracing each ray in the GO principle [4], [5]. The scattered far-field is calculated using a scattered far-field formula derived by the PO integration. This formula is calculated from the information for the last hit points. Therefore, the SBR algorithm consists of two parts—the ray tracing and field calculation parts. The ray-tracing part consumes most of the computation time of the SBR simulation. To reduce the computation time of the ray-tracing part, in this paper, we use the SBR technique based on the uniform spatial subdivision concept [28], [29]. As a result of ray tracing, information for the last hit point of each ray can be obtained [9]. A ray is last reflected at the last hit point and the contribution of the ray to the scattered far-field is calculated using the scattered far-field formula.

Two assumptions are needed to derive the DFT-based ISAR image formula in closed form. The first assumption is that the targets are PEC. From this assumption, the field change with frequency change can be calculated using the scattered far-field formula. The second assumption is that the field is observed at $\phi = 0^\circ$ over $\theta \approx 0^\circ$. This assumption is often referred to as a small angle approximation. Since $\cos \theta \approx 1$ and $\sin \theta \approx \theta$ in the small-angle approximation, the

scattered far-field formula [9] is given by

$$\mathbf{E}^{\mathrm{s}}(f,\theta) = \frac{e^{-jkr}}{r}\left(\hat{\theta}A_\theta + \hat{\phi}A_\phi\right), \tag{1}$$

$$\begin{bmatrix} A_\theta \\ A_\phi \end{bmatrix} = \sum_{i \text{ rays}} \begin{bmatrix} B_\theta \\ B_\phi \end{bmatrix} \left(\frac{jk}{4\pi}\right) (\Delta A)_{\mathrm{exit}}\, S(\theta)\, e^{j\mathbf{k}\cdot\mathbf{r}_A}, \tag{2}$$

$$B_\theta = \begin{bmatrix} \left(-s_1E_3' + s_3E_1' - s_2Z_0H_3' + s_3Z_0H_2'\right) \\ +\theta\left(s_1Z_0H_2' - s_2Z_0H_1'\right) \end{bmatrix} e^{-jkd_i}, \tag{3}$$

$$B_\phi = \begin{bmatrix} \left(-s_2E_3' + s_3E_2' + s_1Z_0H_3' - s_3Z_0H_1'\right) \\ +\theta\left(s_1E_2' - s_2E_1'\right) \end{bmatrix} e^{-jkd_i}, \tag{4}$$

$$B_{\theta,\phi} = (\alpha + \theta\beta)\, e^{-jkd_i}, \tag{5}$$

where r is the distance between the observation point and the target, f is the observation frequency, θ is the observation angle, $\mathbf{k} = k_x\hat{x} + k_y\hat{y} + k_z\hat{z} = k\hat{k}$ is the observation wave number vector, $\mathbf{r}_A$ is the position vector of the last hit point A, $(\Delta A)_{\mathrm{exit}}$ is the cross section of the exit ray tube at the last hit point, and $S(\theta)$ is the shape function, which can usually be assumed to be unity. If the ray tube area is sufficiently small, $\mathbf{E}(A) = \left(E_1'\hat{x} + E_2'\hat{y} + E_3'\hat{z}\right)e^{-jkd_i}$ is the electric field, $\mathbf{H}(A) = \left(H_1'\hat{x} + H_2'\hat{y} + H_3'\hat{z}\right)e^{-jkd_i}$ is the magnetic field at the last hit point, $\hat{s} = s_1\hat{x} + s_2\hat{y} + s_3\hat{z}$ is the exit ray direction, and d_i is the total distance traveled by the i-th ray to the last hit point.

B. MONOSTATIC-BISTATIC EQUIVALENCE PRINCIPLE

The monostatic bistatic equivalence was introduced in [6] in that the radar cross-section can be approximated as a monostatic radar cross-section as the receive and transmit antennas are very close to each other. Consider that a monostatic path and a bistatic path exist for a smooth surface target at a very high frequency as shown in Fig. 1, then the relationship between the monostatic RCS (σ^{mo}) and the bistatic RCS (σ^{bi}) with the incident wave from the $-z$ direction is expressed as [6], [7]

$$\sigma^{\mathrm{mo}}(\theta, f) = \sigma^{\mathrm{bi}}(2\theta, f\cos\theta), \tag{6}$$

Under the small-angle approximation, $\cos\theta \approx 1$ and then (6) can be written as

$$\sigma^{\mathrm{mo}}(\theta, f) = \sigma^{\mathrm{bi}}(2\theta, f). \tag{7}$$

Equation (7) means that the monostatic RCS can be calculated simply from the bistatic RCS. Furthermore, this relationship can also be used to calculate the monostatic scattered far-field from the bistatic scattered far-field. Since the monostatic RCS of (6) and (7) is related to the squared magnitude of the scattered far-field, the phase term must be taken into account for the scattered far-fields. If the last hit point of the i-th ray exists at (x_i, z_i) as shown in Fig. 1, a phase correction term of the i-th ray is given by

$$\Delta\psi_i = 2kz_i\cos\theta + 2kx_i\sin\theta - kz_i(1+\cos 2\theta) - kx_i\sin 2\theta. \tag{8}$$

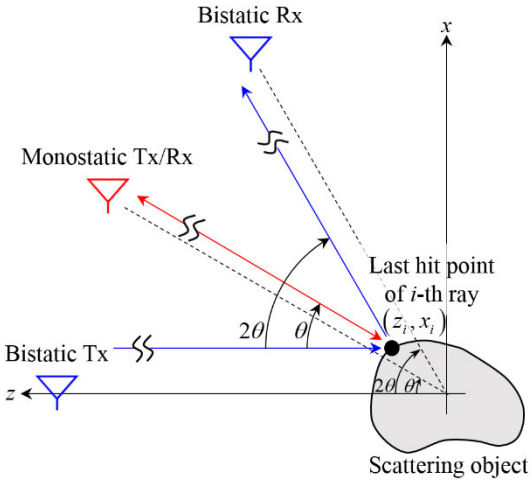

FIGURE 1. Description of the phase difference between the monostatic and bistatic scattered far-field at the last hit point of the i-th ray.

Thus, the monostatic scattered far-field can be calculated using the following formula:

$$\mathbf{E}^{\mathrm{mo}}(f,\theta) = \sum_{i \text{ rays}} \mathbf{E}_i^{\mathrm{bi}}(f, 2\theta)\, e^{j\Delta\psi_i}, \tag{9}$$

where $\mathbf{E}_i^{\mathrm{bi}}$ is the contribution of the i-th ray to the bistatic scattered far-field with the incident wave from the $-z$ direction.

C. APPLYING PARAMETER ESTIMATION METHODS TO SCATTERED FAR-FIELD DATA

For an ISAR image, we use range-corrected monostatic scattered far-field data over M frequencies and N angles [9]. The range-corrected monostatic scattered far-field is given by

$$\tilde{O}_{\theta,\phi}^{\mathrm{mo}}(f,\theta) = \frac{4\pi r}{-jke^{-jkr}} E_{\theta,\phi}^{\mathrm{mo}}(f,\theta), \tag{10}$$

where $E_{\theta,\phi}^{\mathrm{mo}}$ is the monostatic scattered far-field, and the subscript θ or ϕ denotes the corresponding polarization. The unit of the range-corrected scattered far-field is V·m (volt × meter). After obtaining the range-corrected scattered far-field data over M frequencies and N angles, we can apply a parameter estimation method such as MUSIC and ESPRIT, and obtain the super-resolution ISAR image.

The signal structure for the parameter estimation methods is given by

$$Y(m,n) = \sum_i a_i e^{jm\gamma_i + jn\chi_i}. \tag{11}$$

By applying the parameter estimation method to the far-field with the structure of (11), a_i, γ_i, and χ_i can be estimated.

As shown in Fig. 2, the range-corrected monostatic scattered far-field from the scattering centers with the sampling intervals δf and $\delta\theta$ is expressed as

$$\tilde{O}_{\theta,\phi}^{\mathrm{mo}}(f_m,\theta_n) = \sum_i s_i e^{j2k_z z_i + j2k_x x_i}, \tag{12}$$

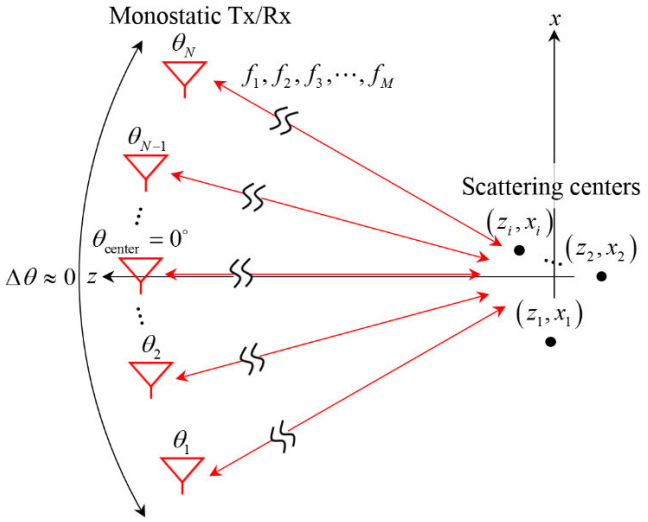

FIGURE 2. Description of the $M \times N$ monostatic scattered far-field data for scattering centers.

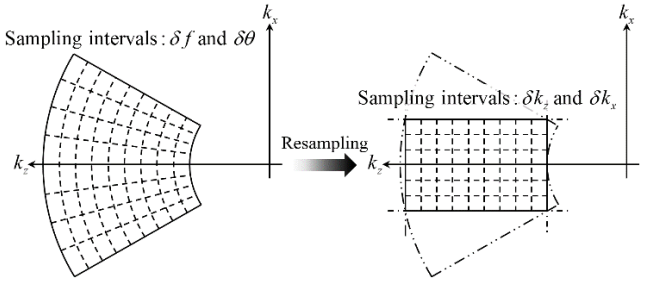

FIGURE 3. Description of resampling the range-corrected monostatic scattered far-field data with the sampling intervals δf and $\delta\theta$ into the field data with sampling intervals δk_z and δk_x.

where $k_z = k\cos\theta$ and $k_x = k\sin\theta$ are the wave number along the z and x directions, respectively, and s_i and (z_i, x_i) are the amplitude and the position of the i-th scattering center, respectively. However, (12) is not matched to the signal structure of (11) because the sampling intervals are not δk_z and δk_x but δf and $\delta\theta$. Therefore, by interpolating the field data with the sampling intervals δf and $\delta\theta$, the field data must be resampled into one with sampling intervals δk_z and δk_x as shown in Fig. 3.

The range-corrected monostatic scattered far-field with the sampling intervals δk_z and δk_x is given by

$$\tilde{O}^{\text{mo}}_{\theta,\phi}\left(k_{z,m}, k_{x,n}\right) = \sum_i s'_i e^{jm2\delta k_z z_i + jn2\delta k_x x_i}, \tag{13}$$

where $s'_i = s_i e^{j2k_{z,0}z_i + j2k_{x,0}x_i}$. Since the field form of (13) with the sampling intervals δk_z and δk_x are matched to the signal structure of (11), scattering centers are extracted and a super-resolution ISAR image is obtained by applying a parameter estimation method to the field data with δk_z and δk_x.

If the field data with δk_z and δk_x are obtained quickly, we can also quickly obtain the super-resolution ISAR image. Therefore, we propose the fast scattered far-field prediction method to obtain the range-corrected monostatic scattered far-field data with the sampling intervals δk_z and δk_x quickly.

III. FAST SCATTERED FAR-FIELD PREDICTION METHOD

In this section, we propose the fast scattered far-field prediction method using the SBR technique, which consists of two parts; the closed-form formula for the DFT-based ISAR image and the field truncation method to suppress the errors caused by the proposed formula.

A. CLOSED-FORM FORMULA FOR THE DFT-BASED ISAR IMAGE

In the previous study, Bhalla [9] derived the FT-based ISAR image formula in closed form to quickly obtain an ISAR image, which is called the image-domain ray-tube integration formula. However, to obtain the range-corrected scattered far-field data from the image-domain ray-tube integration formula, the inverse Fourier transform (IFT) must be performed. It is a more difficult and time-consuming task than using an optimized IDFT code, such as the IFFT function in MATLAB. Even if the field data are obtained using this closed-form formula, there are errors in the field data caused by using this closed-form formula, and the errors have not yet been analyzed.

Therefore, to use the optimized IDFT code and to analyze the errors caused by using the closed-form formula, we use the DFT concept, not the FT concept. That is, we derive the DFT-based ISAR image formula in closed form, which is suitable for quickly obtaining the range-corrected monostatic scattered far-field data with the sampling intervals δk_z and δk_x.

For a PEC target and under the small-angle approximation, where $\theta \approx 0^\circ$ and $\phi = 0^\circ$, the scattered far-field can be calculated using (1)–(5). Thus, the ISAR image using the DFT for the $M \times N$ range-corrected monostatic scattered far-field data with the sampling intervals δk_z and δk_x is expressed as

$$O_{\theta,\phi}(p,q) = \sum_{n=-\frac{N}{2}}^{\frac{N}{2}-1} \sum_{m=-\frac{M}{2}}^{\frac{M}{2}-1} \left[\tilde{O}^{\text{mo}}_{\theta,\phi}\left(k_{z,m}, k_{x,n}\right) \cdot e^{-j2\pi(m/M)p} e^{-j2\pi(n/N)q}\right], \tag{14}$$

where p and q are the down and cross-range bin numbers, respectively, and m and n are the observation k_z and k_x indices, respectively.

By utilizing the MBE principle, we can calculate the range-corrected monostatic scattered far-field $\tilde{O}^{\text{mo}}_{\theta,\phi}$ in (14) from the range-corrected bistatic scattered far-field using (9):

$$\tilde{O}^{\text{mo}}_{\theta,\phi}(f,\theta) = \sum_{i \text{ rays}} \tilde{O}^{\text{bi}}_{\theta,\phi,i}(f, 2\theta)\, e^{j\Delta\psi_i}, \tag{15}$$

$$\tilde{O}^{\text{bi}}_{\theta,\phi,i}(f, 2\theta) = \frac{4\pi r}{-jke^{-jkr}} E^{\text{bi}}_{\theta,\phi,i}(f, 2\theta), \tag{16}$$

where $\tilde{O}^{\text{bi}}_{\theta,\phi,i}$ is the contribution of the i-th ray to the range-corrected bistatic scattered far-field and $E^{\text{bi}}_{\theta,\phi,i}$ is the contribution of the i-th ray to the bistatic scattered far-field

with the incident wave from the $-z$ direction. Equations (1)–(5) and (8) allow us to express (15) as

$$\tilde{O}^{\mathrm{mo}}_{\theta,\phi}(f,\theta) = -\sum_{i\ \mathrm{rays}}\Big[(\Delta A)_{\mathrm{exit}}(\alpha+2\theta\beta) \cdot e^{j\{2kz_i\cos\theta+2kx_i\sin\theta-k(z_i+d_i)\}}\Big]. \quad (17)$$

Under the small-angle approximation, $k \approx k_z$ and $2\theta\beta$ can be ignored. Therefore, in $k_{z,m}$ and $k_{x,n}$ domain, (17) can be rewritten as

$$\tilde{O}^{\mathrm{mo}}_{\theta,\phi}(k_{z,m},k_{x,n}) = -\sum_{i\ \mathrm{rays}}\Big[(\Delta A)_{\mathrm{exit}}\,\alpha e^{j\{k_{z,m}(z_i-d_i)+2k_{x,n}x_i\}}\Big]. \quad (18)$$

Using (18), the range-corrected monostatic scattered far-field data over multiple $k_{z,m}$ and $k_{x,n}$ are calculated through just a one-time ray tracing process at the center frequency and $\theta = 0°$.

To derive the DFT-based ISAR image formula in closed form from (14), the discrete field $\tilde{O}^{\mathrm{mo}}_{\theta,\phi}(k_{z,m},k_{x,n})$ is assumed to be a continuous field $\tilde{O}^{\mathrm{mo}}_{\theta,\phi}(k_z,k_x)$. Then, the summation formula of (14) must be represented as an integration formula:

$$O_{\theta,\phi}(p,q) = -MN\int_{-0.5}^{0.5}\int_{-0.5}^{0.5}\Big[\tilde{O}^{\mathrm{mo}}_{\theta,\phi}(k_z,k_x) \cdot e^{-j2\pi m'p}e^{-j2\pi n'q}dm'dn', \quad (19)$$

where $k_z = k_{z0} + \Delta k_z m'$, $k_x = \Delta k_x n'$, k_{z0} is the center k_z, Δk_z is the k_z bandwidth, and Δk_x is the k_x bandwidth. Substituting (18) into (19) gives

$$O_{\theta,\phi}(p,q) = -MN\sum_{i\ \mathrm{rays}}\Bigg[\alpha(\Delta A)_{\mathrm{exit}}e^{jk_{z0}(z_i-d_i)} \cdot\left(\int_{-0.5}^{0.5}e^{-jm'\{2\pi p-\Delta k_z(z_i-d_i)\}}dm'\right) \cdot\left(\int_{-0.5}^{0.5}e^{-jn'(2\pi q-2\Delta k_x x_i)}dn'\right)\Bigg]. \quad (20)$$

The integrations can be easily carried out analytically. Therefore, the closed-form formula for the DFT-based ISAR image is given by

$$O_{\theta,\phi}(p,q) = -MN\sum_{i\ \mathrm{rays}}\Bigg[\alpha(\Delta A)_{\mathrm{exit}}e^{jk_{z0}(z_i-d_i)} \cdot\mathrm{sinc}\left(\pi p-\Delta k_z\frac{z_i-d_i}{2}\right)\cdot\mathrm{sinc}(\pi q-\Delta k_x x_i)\Bigg], \quad (21)$$

where $\mathrm{sinc}(u) = \sin(u)/u$. For more intuitive understanding, (21) can be expressed in terms of the down-range z and the cross-range x:

$$O_{\theta,\phi}(z,x) = -MN\sum_{i\ \mathrm{rays}}\Bigg[\alpha(\Delta A)_{\mathrm{exit}}e^{jk_{z0}(z_i-d_i)} \cdot\mathrm{sinc}\left\{\Delta k_z\left(z-\frac{z_i-d_i}{2}\right)\right\}\cdot\mathrm{sinc}\{\Delta k_x(x-x_i)\}\Bigg], \quad (22)$$

where $z = \pi p/\Delta k_z$, $x = \pi q/\Delta k_x$, the down-range resolution $\delta z = \pi/\Delta k_z$, and the cross-range resolution $\delta x = \pi/\Delta k_x$. After ray tracing is performed only once at the center frequency and $\theta = 0°$, the DFT-based ISAR image is obtained quickly by using the proposed formula of (22), and also the range-corrected monostatic scattered far-field data with the sampling intervals δk_z and δk_x are obtained quickly by inverse discrete Fourier transforming this image.

B. FIELD TRUNCATION METHOD TO SUPPRESS THE ERRORS CAUSED BY THE PROPOSED FORMULA

Approximating the summation formula of (14) as the integration formula of (19) generates errors in the field data. Therefore, we propose the field truncation method to suppress these errors in the field data caused by the proposed formula of (22).

Because two variables k_z and k_x are independent in (20), the analysis of the errors in the 1D DFT-based range profile (RP) domain directly expands into the analysis of the errors in the 2D DFT-based ISAR image domain.

Consider the 1D case in which $\theta = 0°$, $k_m = k_{z,m}$, and m is the observation k index. The DFT-based RP over M wave numbers is expressed as

$$RP_{\theta,\phi}(p) = \sum_{m=-\frac{M}{2}}^{\frac{M}{2}-1}\tilde{O}_{\theta,\phi}(k_m)\,e^{-j2\pi(m/M)p}, \quad (23)$$

where $\tilde{O}_{\theta,\phi}(k_m)$ is the range-corrected scattered far-field, and the approximated integration formula is given by

$$RP_{\theta,\phi}(p) = M\int_{-0.5}^{0.5}\tilde{O}_{\theta,\phi}(k)\,e^{-j2\pi m'p}dm'. \quad (24)$$

The difference between (23) and (24) is the error in the RP domain, and each l-th field at k_l causes a l-th error in the RP domain. The l-th error in the RP domain is expressed as

$$\mathrm{error}_{\mathrm{RP},l}(p) = 2\sum_{i\ \mathrm{rays}}\Bigg[\alpha(\Delta A)_{\mathrm{exit}}e^{jk_0(z_i-d_i)-j\frac{l}{M}\{2\pi p-\Delta k(z_i-d_i)\}} -\alpha(\Delta A)_{\mathrm{exit}}M\int_{\frac{l}{M}}^{\frac{l+1}{M}}e^{jk(z_i-d_i)-jm'\{2\pi p-\Delta k(z_i-d_i)\}}dm'\Bigg], \quad (25)$$

where α is brought from (5). The integration in (25) can be carried out analytically; therefore, the closed-form expression of the l-th error in the RP domain is given by

$$\mathrm{error}_{\mathrm{RP},l}(p) = 2\sum_{i\ \mathrm{rays}}\alpha(\Delta A)_{\mathrm{exit}}e^{jk_0(z_i-d_i)-j\frac{l}{M}\{2\pi p-\Delta k(z_i-d_i)\}}$$

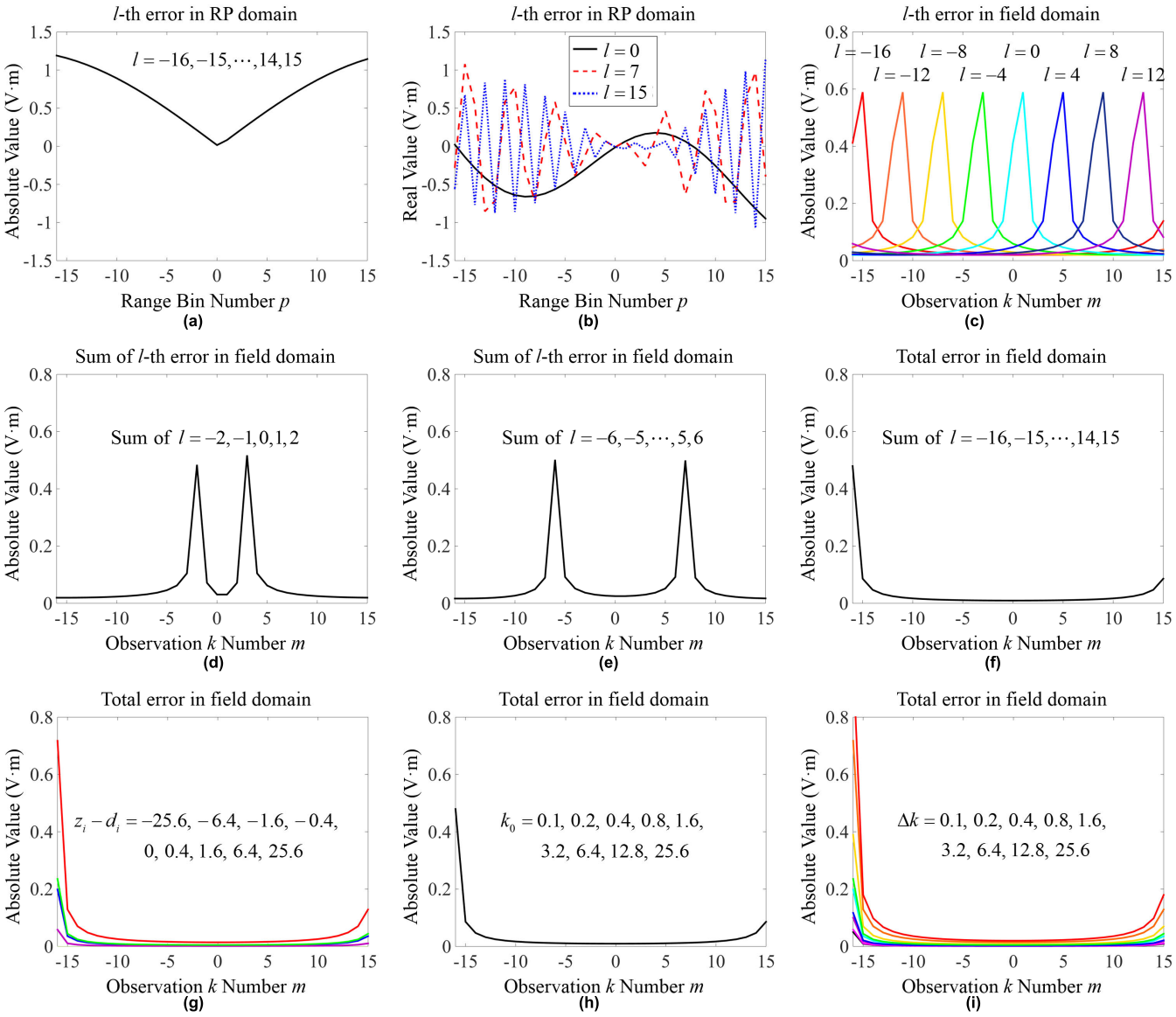

FIGURE 4. The analysis of the errors of just one ray caused by using the proposed formula (22) with $\alpha(\Delta A)_{\text{exit}} = 1$, $z_i - d_i = 1$, $k_0 = 1$, $\Delta k = 1$, and $M = 32$. (a) The absolute value of the l-th error in the RP domain at $l = -16, -15, \ldots, 14, 15$. (b) The real value of the l-th error in the RP domain at $l = 0, 7, 15$. (c) The l-th error in the field domain at $l = -16, -12, \ldots, 8, 12$. (d) The sum of the l-th error in the field domain over $l = -2, -1, 0, 1, 2$. (e) The sum of the l-th error in the field domain over $l = -6, -5, \ldots, 5, 6$. (f) The total error in the field domain. (g) The total error in the field domain at $z_i - d_i = -25.6, -6.4, -1.6, -0.4, 0, 0.4, 1.6, 6.4, 25.6$. (h) The total error in the field domain at $k_0 = 0.1, 0.2, 0.4, 0.8, 1.6, 3.2, 6.4, 12.8, 25.6$. (i) The total error in the field domain at $\Delta k = 0.1, 0.2, 0.4, 0.8, 1.6, 3.2, 6.4, 12.8, 25.6$.

$$\cdot \left[1 - \text{sinc}\left[\frac{1}{2M}\{2\pi p - \Delta k\,(z_i - d_i)\}\right] \times e^{-j\frac{1}{2M}[2\pi p - \Delta k(z_i - d_i)]}\right]. \tag{26}$$

The total error in the RP domain is expressed as a sum of the l-th errors in the RP domain:

$$\text{error}_{\text{RP}}(p) = \sum_{l=-\frac{M}{2}}^{\frac{M}{2}-1} \text{error}_{\text{RP},l}(p). \tag{27}$$

The l-th error in the RP domain can be calculated using (26), and by inverse discrete Fourier transforming these, the l-th error in the field domain can be obtained. As a result, we can obtain the total error in the field domain by summing the l-th error in the field domain. Fig. 4 shows the errors of just one ray with $\alpha(\Delta A)_{\text{exit}} = 1, z_i - d_i = 1, k_0 = 1, \Delta k = 1$, and $M = 32$ in (26). Each l-th error in the RP domain has the same amplitude and different phase as shown in Figs. 4(a) and 4(b). It causes the l-th errors in the field domain to be transformed parallel to the same shape and also to have a peak near $m = l$, as shown in Fig. 4(c).

As shown in Figs. 4(d)–(f), each l-th error is suppressed when each error is summed. Therefore, the total error in the field domain has a large value near $m = -M/2$ and $m = M/2 - 1$, and a low value in the rest of m as shown in Fig. 4(f). This property remains even if $z_i - d_i$, k_0, and Δk change into any value as shown in Figs. 4(g)–(i). Therefore, in all cases,

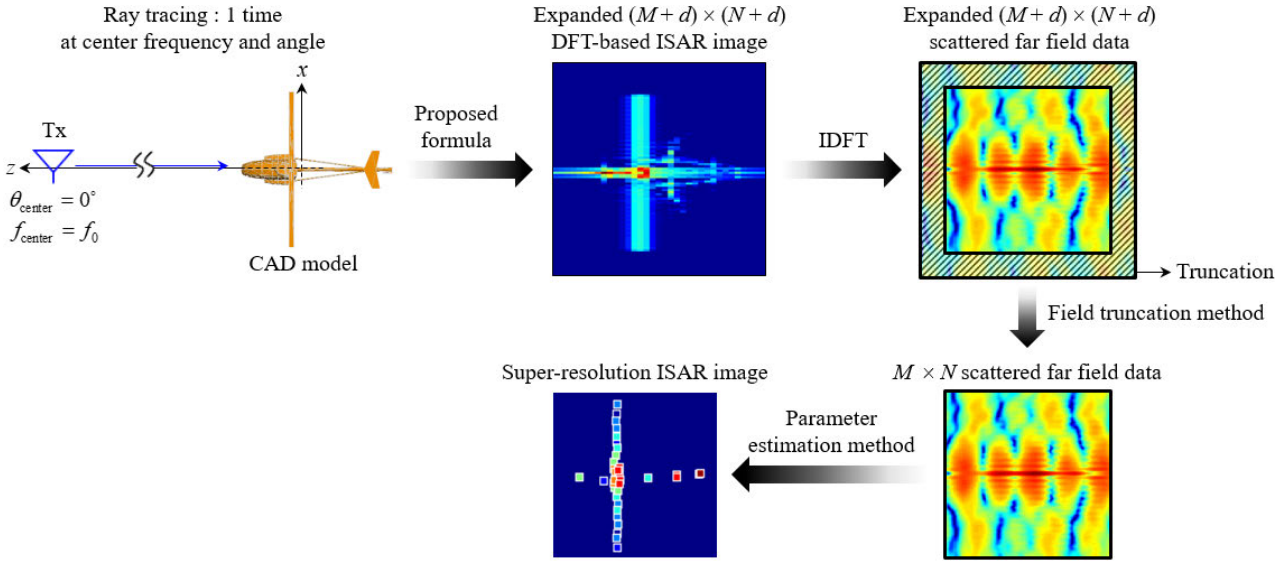

FIGURE 5. Description of the proposed fast scattered far-field prediction method for super-resolution ISAR image formation.

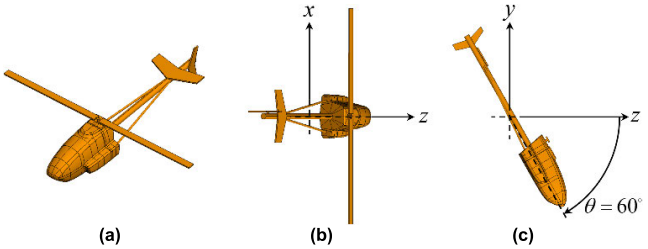

FIGURE 6. CAD model of a helicopter. (a) Target geometry. (b) Target orientation view in the *zx*-plane. (c) Target orientation view in the *yz*-plane.

the total error of any ray in the field domain has a high value near both ends of m and a low value in the rest of m. This property directly expands into the 2D DFT-based ISAR image case, so we propose the field truncation method to suppress the errors caused by using the proposed DFT-based ISAR image formula of (22).

Fig. 5 shows the application procedure of the proposed DFT-based ISAR image formula and the field truncation method. When we obtain the $M \times N$ field data with k_{z0}, Δk_z, and Δk_x, we first obtain the expanded $(M+d) \times (N+d)$ field data with k_{z0}, $\Delta k_z' = (M+d)\,\Delta k_z / M$, and $\Delta k_x' = (N+d)\,\Delta k_x / N$ using the proposed DFT-based ISAR image formula of (22). Here, d is the number of truncations, and the expanded $(M+d) \times (N+d)$ field data contain the $M \times N$ field data. Then, by truncating the field data as much as d near both ends of m and n, we quickly obtain the $M \times N$ field data with low errors.

IV. RESULTS AND DISCUSSIONS

In this section, for PEC CAD models, we obtain $M \times N$ range-corrected monostatic scattered far-field data and super-resolution ISAR images using the conventional method and the proposed method. In these simulations, the range-corrected monostatic scattered far-field is obtained from one-time ray tracing process at the center frequency and angle, which is implemented in C language and validated from our previous studies [30]–[32]. The incident plane waves have an amplitude of 1 V/m, and the ESPRIT algorithm [25], [26] is used to obtain a super-resolution ISAR image. By comparing the results of the proposed method to those of the conventional method, we verify the performance of the proposed method. Simulations are performed on a personal computer (Intel Core i5-760 CPU @ 2.80 GHz, 8 GB RAM).

A. HELICOPTER CAD MODEL

Fig. 6 shows the geometry and orientation of the perfectly conducting helicopter CAD model, which is tilted at an angle of $\theta = 60°$ and $\phi = -90°$. The dimensions (length × width × height) are 16 m × 16 m × 3 m. The range-corrected monostatic scattered far-field data are computed using the conventional method over 128 frequencies and 128 angles with a 5 GHz center frequency, a 0.5 GHz frequency bandwidth, and an observation angle varying from $\theta = -2°$ to $\theta = 2°$ at $\phi = 0°$.

In the conventional method, the 128 × 128 field data are obtained through 128-time ray tracing processes and 128 × 128-time field calculations. The field data with the sampling intervals δf and $\delta\theta$ are resampled into ones with the sampling intervals δk_z and δk_x. The resampled 128 × 128 field data have $k_{z0} = 104.6522$ /m, $\Delta k_z = 10.3369$ /m, and $\Delta k_x = 6.8394$ /m. On the other hand, in the proposed method, ray tracing is performed only once at 5 GHz and $\theta = 0°$. Then, the expanded 144 × 144 DFT-based ISAR image is obtained using the proposed formula of (22), and the 128 × 128 DFT-based ISAR image is obtained using the field truncation method. By inverse discrete Fourier transforming this image, the 128 × 128 field data are obtained.

Fig. 7 shows the simulation results, and the computation times are summarized in Table 1. The conventional method takes 6 h, while the proposed method takes 107 s to obtain the range-corrected monostatic scattered far-field data with

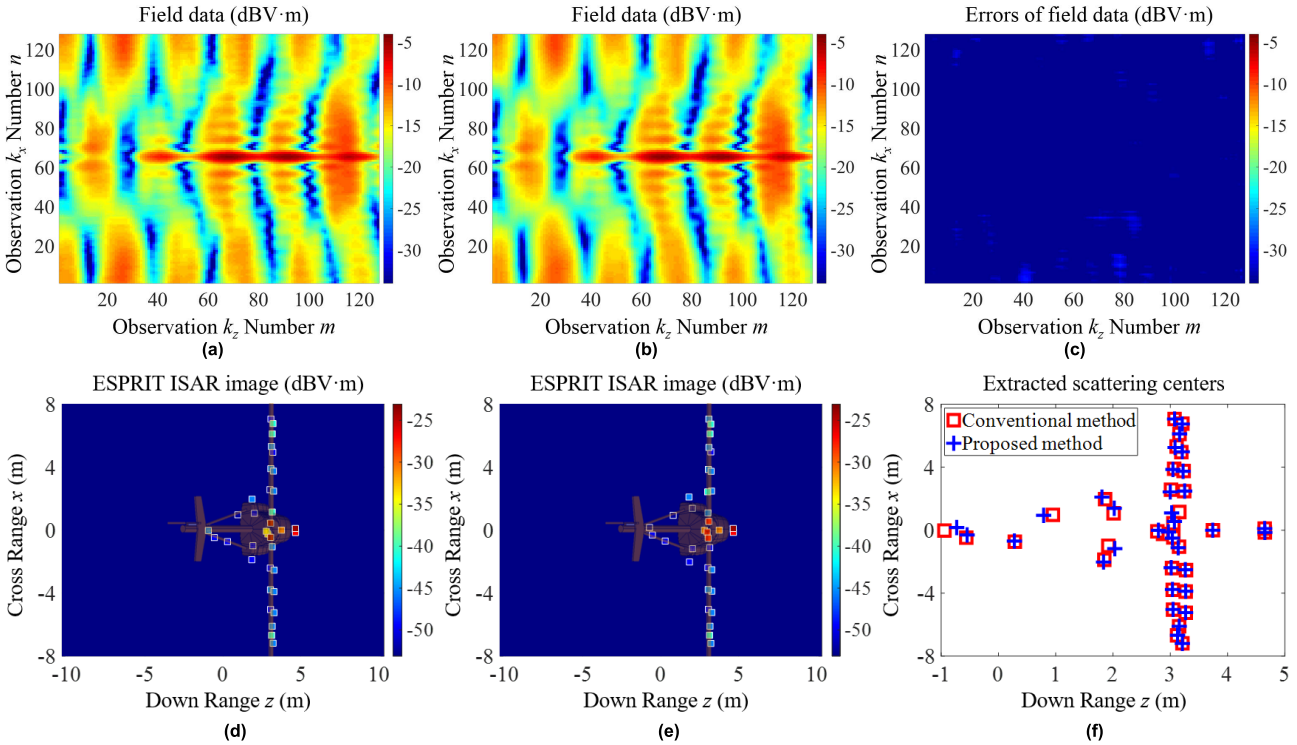

FIGURE 7. The simulation results for the helicopter CAD model. (a) The range-corrected monostatic scattered far-field data using the conventional method. (b) The range-corrected monostatic scattered far-field data using the proposed method. (c) The errors in the range-corrected monostatic scattered far-field data using the proposed method. (d) The ESPRIT ISAR image using the conventional method. (e) The ESPRIT ISAR image using the proposed method. (f) The scattering centers extracted from the two methods.

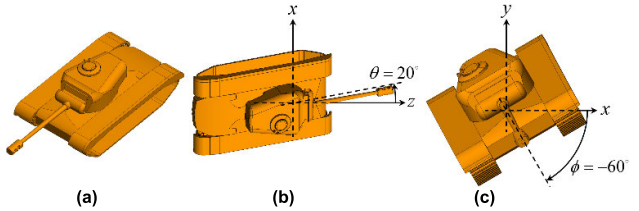

FIGURE 8. CAD model of a tank. (a) Target geometry. (b) Target orientation view in the *zx*-plane. (c) Target orientation view in the *xy*-plane.

TABLE 1. Computation time of the range-corrected monostatic scattered far-field data for two cad models using the conventional method and the proposed method.

CAD	Process	Conventional method	Proposed method
Helicopter model	CAD input	3 s	3 s
	Ray tracing	9,476 s	74 s
	Field calculation	12,137 s	30 s
	Total time	21,616 s (6 h)	107 s
Tank model	CAD input	9 s	9 s
	Ray tracing	10,590 s	84 s
	Field calculation	29,492 s	39 s
	Total time	40,091 s (11.14 h)	132 s

the sampling intervals δk_z and δk_x in Figs. 7(a) and 7(b). The proposed method tremendously reduces the computation time. In particular, since the conventional method performs 128-time ray-tracing processes for 128 angles, while the proposed method performs ray tracing once at one angle, the ray-tracing calculation time is shortened. In addition, while the conventional method calculates 128 × 128 fields, the proposed method calculates fields only through the proposed formula of (22), the truncation process, and inverse discrete Fourier transformation, so the field calculation time is greatly reduced.

The errors, which are the differences in the field data between the two methods, have low values as shown in Fig. 7(c). The maximum absolute value of the errors is 0.0339 V·m, the average is 0.0097 V·m, and the root mean square (RMS) is 0.0111 V·m, although the maximum and the average absolute value of the resampled field data using the conventional method is 0.6032 V·m and 0.1462 V·m, respectively. It takes about 8 s to apply ESPRIT to the field data, and Figs. 7(d)-(f) show the applied results.

The scattering property of the helicopter CAD model is represented as scattering centers in Figs. 7(d) and 7(e). The errors cause differences in the ISAR image, but the differences in the scattering centers between the two methods are small as shown in Fig. 7(f). In particular, strong scattering centers obtained using the proposed method are in good agreement with those using the conventional method. These results confirm that the proposed method is a very efficient way to obtain the range-corrected monostatic scattered far-field data and super-resolution ISAR images.

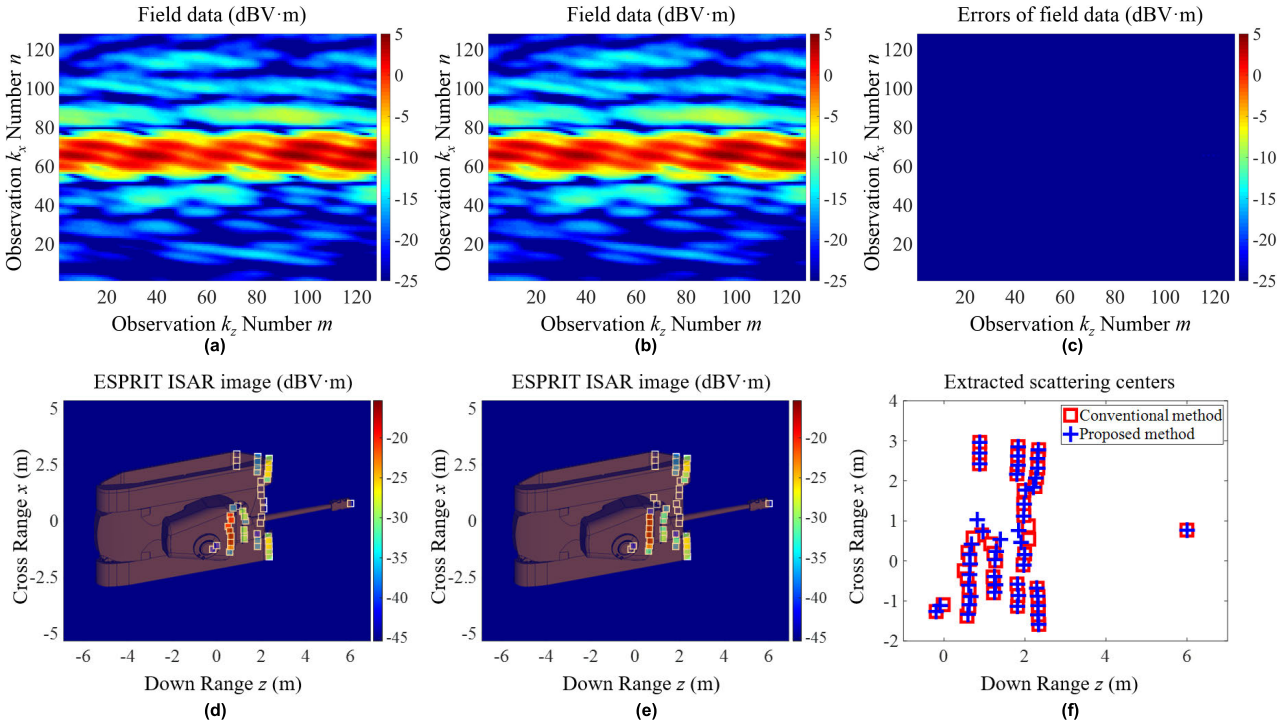

FIGURE 9. The simulation results for the tank CAD model. (a) The range-corrected monostatic scattered far-field data using the conventional method. (b) The range-corrected monostatic scattered far-field data using the proposed method. (c) The errors in the range-corrected monostatic scattered far-field data using the proposed method. (d) The ESPRIT ISAR image using the conventional method. (e) The ESPRIT ISAR image using the proposed method. (f) The scattering centers extracted from the two methods.

B. TANK CAD MODEL

The second CAD model is a perfectly conducting tank, and Fig. 8 shows the geometry and the orientation of the CAD model, which is tilted at an angle of $\theta = 20°$ and $\phi = 300°$. The dimensions (length × width × height) of the tank CAD model are 8.8 m (12.2 m with cannon) × 5.2 m × 3.5 m.

The range-corrected monostatic scattered far-field data are computed using the conventional method over 128 frequencies and 128 angles with a 10 GHz center frequency, a 0.4 GHz frequency bandwidth, and an observation angle varying from $\theta = -2.8°$ to $\theta = 2.8°$ at $\phi = 0°$.

In the conventional method, the 128 × 128 field data are obtained through 128-times ray tracing processes and 128 × 128-times field calculations over 128 frequencies and 128 angles, and they are resampled into the field data with the sampling intervals δk_z and δk_x. In the proposed method, ray tracing is performed only once at 10 GHz and $\theta = 0°$. Then, the expanded 144 × 144 DFT-based ISAR image and the 128 × 128 DFT-based ISAR image are consecutively obtained using the proposed formula of (22) and the field truncation method. Finally, the 128 × 128 field data are also obtained by inverse discrete Fourier transformation.

Table 1 and Fig. 9 show the simulation results. The conventional method takes 11.14 h, while the proposed method takes 132 s to obtain the range-corrected monostatic scattered far-field data with the sampling intervals δk_z and δk_x in Figs. 9(a) and 9(b). This result means that the higher the frequency and the more complex the structure, the more effective the proposed method is. The errors in the field data also have a very low level as shown in Fig. 9(c). The maximum, average, and RMS of the errors are 0.0649 V·m, 0.0139 V·m, and 0.0161 V·m, respectively. Considering that the maximum absolute value of the field data using the conventional method is 1.7598 V·m, the errors are very small. It takes about 8 s to apply ESPRIT to the field data, and the results are shown in Figs. 9(d)–(f). The scattering property of the tank CAD model is represented as scattering centers in Figs. 9(d) and 9(e). Unlike the helicopter model, in both the conventional and proposed methods, most of the incident fields are reflected from the front part of the tank, so the scattering centers are also concentrated on the front part of the tank. The errors cause differences in the ISAR image. The differences in the scattering centers between the two methods are concentrated near $z = 1$ m and $x = 0$ m, but these are small as shown in Fig. 9(f). These results confirm that the proposed method also works very well for the range-corrected monostatic scattered far-field data and super-resolution ISAR images at a higher frequency.

V. CONCLUSION

In this paper, we proposed the fast scattered far-field prediction method for obtaining a super-resolution ISAR image for a complex PEC CAD model using the SBR technique. The DFT-based ISAR image formula is derived in closed form and the field truncation method is proposed to suppress errors caused by using the derived closed-form formula. Using this closed-form formula and the field truncation method, we quickly obtained the range-corrected scattered far-field

data with the sampling intervals δk_z and δk_x, which have few errors. By applying a parameter estimation method to the field data, we obtained the super-resolution ISAR image. To verify the proposed method, we simulated helicopter and tank CAD models. The results of the proposed method were good agreement with those of the conventional method, although the proposed method tremendously reduced the computation times. These results confirm that the proposed method is a very efficient way to obtain the range-corrected scattered far-field data and super-resolution ISAR images.

REFERENCES

[1] T. D. Ross, S. W. Worrell, V. J. Velten, J. C. Mossing, and M. L. Bryant, "Standard SAR ATR evaluation experiments using the MSTAR public release data set," *Proc. SPIE*, vol. 3370, pp. 566–573, Sep. 1998.

[2] E. R. Keydel and S. W. Lee, "Signature prediction for model-based automatic target recognition," *Proc. SPIE*, vol. 2757, pp. 306–317, Apr. 1996.

[3] C. Özdemir, *Inverse Synthetic Aperture Radar Imaging With MATLAB Algorithms*. Hoboken, NJ, USA: Wiley, 2012.

[4] H. Ling, R.-C. Chou, and S.-S. Lee, "Shooting and bouncing rays: Calculating the RCS of an arbitrarily shaped cavity," *IEEE Trans. Antennas Propag.*, vol. 37, no. 2, pp. 194–205, Feb. 1989.

[5] S. W. Lee, H. Ling, and R. C. Chou, "Ray tube integration in shooting and bouncing ray method," *Microw. Opt. Tech. Lett.*, vol. 1, pp. 285–289, Oct. 1988.

[6] R. E. Kell, "On the derivation of bistatic RCS from monostatic measurements," *Proc. IEEE*, vol. 53, no. 8, pp. 983–988, Aug. 1965.

[7] H. Buddendick and T. F. Eibert, "Acceleration of ray-based radar cross section predictions using monostatic-bistatic equivalence," *IEEE Trans. Antennas Propag.*, vol. 58, no. 2, pp. 531–539, Feb. 2010.

[8] H. Ling and R. Bhalla, "Time-domain ray-tube integration formula for the shooting-and-bouncing-ray technique," Univ. Texas Austin, Austin, TX, USA, Tech. Rep. NASA Grant NCC 3-273, 1993.

[9] R. Bhalla and H. Ling, "Image domain ray tube integration formula for the shooting and bouncing ray technique," *Radio Sci.*, vol. 30, no. 5, pp. 1435–1446, Sep./Oct. 1995.

[10] R. Bhalla and H. Ling, "A fast algorithm for signature prediction and image formation using the shooting and bouncing ray technique," *IEEE Trans. Antennas Propag.*, vol. 43, no. 7, pp. 727–731, Jul. 1995.

[11] R. Bhalla and H. Ling, "Three-dimensional scattering center extraction using the shooting and bouncing ray technique," *IEEE Trans. Antennas Propag.*, vol. 44, no. 11, pp. 1445–1453, Nov. 1996.

[12] R. Bhalla, H. Ling, J. Moore, D. J. Andersh, S. W. Lee, and J. Hughes, "3D scattering center representation of complex targets using the shooting and bouncing ray technique: A review," *IEEE Antennas Propag. Mag.*, vol. 40, no. 5, pp. 30–39, Oct. 1998.

[13] X.-Y. He, X.-B. Wang, X. Zhou, B. Zhao, and T.-J. Cui, "Fast ISAR image simulation of targets at arbitrary aspect angles using a novel SBR method," *Prog. Electromagn. Res. B*, vol. 28, pp. 129–142, 2011.

[14] X. Y. He, X. Y. Zhou, and T. J. Cui, "Fast 3D-ISAR image simulation of targets at arbitrary aspect angles through nonuniform fast Fourier transform (NUFFT)," *IEEE Trans. Antennas Propag.*, vol. 60, no. 5, pp. 2597–2602, May 2012.

[15] D. J. Yun, J. I. Lee, K. U. Bae, K. I. Kwon, and N. H. Myung, "Improvement in accuracy of ISAR image formation using the shooting and bouncing ray," *IEEE Antennas Wireless Propag. Lett.*, vol. 14, pp. 970–973, 2015.

[16] A. Segalovitz and B. R. Frieden, "A CLEAN-type deconvolution algorithm," *Astron. Astrophys.*, vol. 70, pp. 335–343, Nov. 1978.

[17] J. Tsao and B. D. Steinberg, "Reduction of sidelobe and speckle artifacts in microwave imaging: The CLEAN technique," *IEEE Trans. Antennas Propag.*, vol. AP-36, no. 4, pp. 543–556, Apr. 1988.

[18] R. Bose, A. Freedman, and B. D. Steinberg, "Sequence CLEAN: A modified deconvolution technique for microwave images of continuous targets," *IEEE Trans. Aerosp. Electron. Syst.*, vol. 38, no. 1, pp. 89–96, Jan. 2002.

[19] P. T. Gough, "A fast spectral estimation algorithm based on the FFT," *IEEE Trans. Signal Process.*, vol. 42, no. 6, pp. 1317–1322, Jun. 1994.

[20] J. Li and P. Stoica, "Efficient mixed-spectrum estimation with applications to target feature extraction," *IEEE Trans. Signal Process.*, vol. 44, no. 2, pp. 281–295, Feb. 1996.

[21] R. O. Schmidt, "Multiple emitter location and signal parameter estimation," *IEEE Trans. Antennas Propag.*, vol. AP-34, no. 3, pp. 276–280, Mar. 1986.

[22] R. Roy and T. Kailath, "Esprit-estimation of signal parameters via rotational invariance techniques," *IEEE Trans. Acoust., Speech, Signal Process.*, vol. 37, no. 7, pp. 984–995, Jul. 1989.

[23] J. W. Odendaal, E. Barnard, and C. W. I. Pistorius, "Two-dimensional superresolution radar imaging using the MUSIC algorithm," *IEEE Trans. Antennas Propag.*, vol. 42, no. 10, pp. 1386–1391, Oct. 1994.

[24] K.-T. Kim, S.-W. Kim, and H.-T. Kim, "Two-dimensional ISAR imaging using full polarization and super-resolution processing techniques," *Proc. Inst. Elect. Eng. Radar, Sonar Navig.*, vol. 145, no. 4, pp. 240–246, Aug. 1998.

[25] Y. Wang and H. Ling, "A frequency-aspect extrapolation algorithm for ISAR image simulation based on two-dimensional ESPRIT," *IEEE Trans. Geosci. Remote Sens.*, vol. 38, no. 4, pp. 1743–1748, Jul. 2000.

[26] M. L. Burrows, "Two-dimensional ESPRIT with tracking for radar imaging and feature extraction," *IEEE Trans. Antennas Propag.*, vol. 52, no. 2, pp. 524–532, Feb. 2004.

[27] A. B. Constantine, *Antenna Theory Analysis and Design*. Hoboken, NJ, USA: Wiley, 2005.

[28] J. G. Cleary and G. Wyvill, "Analysis of an algorithm for fast ray tracing using uniform space subdivision," *Vis. Comput.*, vol. 4, no. 2, pp. 65–83, Mar. 1988.

[29] A. Woo, "Ray tracing polygons using spatial subdivision," in *Proc. Conf. Graph. Interface*, vol. 92, 1992, pp. 184–191.

[30] J.-I. Lee and D.-W. Seo, "Improvement of computational efficiency for fast ISAR image simulation through nonuniform fast Fourier transform," *IEEE Antennas Wireless Propag. Lett.*, vol. 20, no. 12, pp. 2402–2406, Dec. 2021, doi: 10.1109/LAWP.2021.3113314.

[31] J.-I. Lee, D.-J. Yun, H.-J. Kim, W.-Y. Yang, and N.-H. Myung, "Fast ISAR image formations over multiaspect angles using the shooting and bouncing rays," *IEEE Antennas Wireless Propag. Lett.*, vol. 17, no. 6, pp. 1020–1023, Jun. 2018, doi: 10.1109/LAWP.2018.2829826.

[32] D.-J. Yun, J.-I. Lee, K.-U. Bae, J.-H. Yoo, K.-I. Kwon, and N.-H. Myung, "Improvement in computation time of 3-D scattering center extraction using the shooting and bouncing ray technique," *IEEE Trans. Antennas Propag.*, vol. 65, no. 8, pp. 4191–4199, Aug. 2017, doi: 10.1109/TAP.2017.2708078.

JAE-IN LEE received the B.S. degree in electrical engineering from Kyungpook National University, Daegu, South Korea, in 2012, and the Ph.D. degree in electrical engineering from the Korea Advanced Institute of Science and Technology (KAIST), Daejeon, South Korea, in 2019. He is currently a Postdoctoral Researcher with the Interdisciplinary Major of Maritime AI Convergence, Korea Maritime and Ocean University (KMOU), Busan, South Korea. His research interests include numerical techniques in areas of electromagnetics, radar cross-section analysis, and inverse synthetic aperture radar imaging.

DONG-WOOK SEO (Senior Member, IEEE) received the B.S. degree in electrical engineering from Kyungpook National University, Daegu, South Korea, in 2003, and the M.S. and Ph.D. degrees in electrical engineering from the Korea Advanced Institute of Science and Technology (KAIST), Daejeon, South Korea, in 2005 and 2011, respectively. He was a Senior Researcher with the Defense Agency for Technology and Quality (DTaQ), Daegu, from 2011 to 2012. From 2012 to 2017, he was a Senior Researcher with the Electronics and Telecommunications Research Institute (ETRI), Daegu. Since September 2017, he has been with Korea Maritime and Ocean University (KMOU), Busan, South Korea, where he is currently an Associate Professor with the Division of Electronics and Electrical Information Engineering. His current research interests include numerical techniques in areas of electromagnetics, radar cross-section analysis, wireless power transfer, and radar systems.